

---

# Hiding in Plain Sight: Disguising Data Stealing Attacks in Federated Learning

---

**Kostadin Garov**

INSAIT

Sofia University

Sofia, Bulgaria

[kostadin.garov@insait.ai](mailto:kostadin.garov@insait.ai)

**Dimitar I. Dimitrov**

Department of Computer Science

ETH Zurich

Zurich, Switzerland

[dimitar.iliev.dimitrov@inf.ethz.ch](mailto:dimitar.iliev.dimitrov@inf.ethz.ch)

**Nikola Jovanović**

Department of Computer Science

ETH Zurich

Zurich, Switzerland

[nikola.jovanovic@inf.ethz.ch](mailto:nikola.jovanovic@inf.ethz.ch)

**Martin Vechev**

Department of Computer Science

ETH Zurich

Zurich, Switzerland

[martin.vechev@inf.ethz.ch](mailto:martin.vechev@inf.ethz.ch)

## Abstract

Malicious server (MS) attacks have enabled the scaling of data stealing in federated learning to large batch sizes and secure aggregation, settings previously considered private. However, many concerns regarding client-side detectability of MS attacks were raised, questioning their practicality once they are publicly known. In this work, for the first time, we thoroughly study the problem of client-side detectability. We demonstrate that most prior MS attacks, which fundamentally rely on one of two key principles, are detectable by principled client-side checks. Further, we formulate desiderata for practical MS attacks and propose SEER, a novel attack framework that satisfies all desiderata, while stealing user data from gradients of realistic networks, even for large batch sizes (up to 512 in our experiments) and under secure aggregation. The key insight of SEER is the use of a secret decoder, which is jointly trained with the shared model. Our work represents a promising first step towards more principled treatment of MS attacks, paving the way for realistic data stealing that can compromise user privacy in real-world deployments.

## 1 Introduction

Federated learning [1] (FL) was proposed as a way to train machine learning models while preserving privacy and is increasingly being deployed in real-world systems [2, 3, 4]. In FL, a *server* trains a *shared model* by applying aggregated gradient updates, received from a large number of *clients*.

**Gradient leakage attacks** A long line of work [5, 6, 7, 8, 9, 10], primarily on images, has shown that even passive servers can reconstruct client data from gradients, breaking the key privacy promise of FL. However, these attacks are only applicable to naive FL deployments [11]—in real-life settings with no unrealistic assumptions, they are limited to small batch sizes with no secure aggregation [12]. In response, recent work has argued that the honest-but-curious threat model underestimates the risks of FL, as real-world servers can be malicious or compromised. This led to *malicious server (MS)* attacks, which have demonstrated promising results by lifting honest attacks to large batch sizes.

Most prior MS attacks rely on one of two key underlying principles. One attack class [13, 14, 15, 16] uses malicious model modifications to encourage different types of sparsity in dense layer gradients, enabling the application of analytical honest attacks—we refer to these attacks as *boosted analytical*.

Other attacks utilize *example disaggregation* [17, 18], reducing the effective batch size in the gradient space by restricting the gradient flow, which permits the use of optimization-based honest attacks.

**Client-side detectability** Nearly all prior work in the field [8, 13, 14, 15, 19, 17, 18, 20] has raised the issue of *client-side detectability* of MS attacks, i.e., an FL client may be able to detect malicious server activity, and decide to opt out of the current or all future rounds. Despite such concerns, no attempts have so far been made to study, quantify, or improve client-side detectability of MS attacks.

**This work: detecting and disguising malicious server attacks** In this work, we thoroughly study the question of client-side detectability of MS attacks. We demonstrate that while boosted analytical and example disaggregation attacks pose a real threat as zero-day exploits, now that their key principles are known, *all* current (and future) attacks from these two classes are client-side detectable in a principled way, bringing into question their practicality. Notably, we demonstrate the detectability of example disaggregation attacks by introducing D-SNR, a novel vulnerability metric.

With this in mind, we observe that such limitations of prior MS attacks arise from their fundamental reliance on the honest attacks they lift. Namely, boosted analytical attacks always require handcrafted modifications which are *weight-space detectable*, and example disaggregation attacks rely on the success of disaggregation, which is equally evident to any party observing the gradients, i.e., it is *gradient-space detectable*. This illustrates the need for fundamentally different attack approaches.

As a promising first step in that direction, we propose a novel attack framework SEER, which recovers data from batch sizes up to 512, yet is by design harder to detect than prior attacks. Our key insights are that (i) gradient-space detection can be evaded using a *secret decoder*, disaggregating the data in a space unknown to clients, and (ii) jointly optimizing the decoder and the shared model with SGD *avoids handcrafted modifications* and allows for effective reconstruction. Importantly, SEER does not lift any prior honest attack and does not require restrictive assumptions such as the ability to tweak the architecture, side-channel information, or knowledge of batch normalization data or labels.

**Key contributions** Our work makes the following contributions.

- In Sec. 3, we demonstrate that both boosted analytical and example disaggregation MS attacks are detectable using principled checks—for the latter, we introduce D-SNR, a novel gradient-space metric of data vulnerability that additionally protects clients from unintended leakage. We formulate the main desiderata for realistic MS attacks and make the case that detection should become a key concern when designing future attacks.
- In Sec. 4, we propose a novel attack framework, SEER, based on malicious fine-tuning of the shared model along with a secret server-side decoder, which satisfies all desiderata, and is by design harder to detect as it does not rely on honest attacks, avoiding previous pitfalls.
- Finally, in Sec. 5, we present an extensive experimental evaluation of SEER on several datasets and realistic network architectures, demonstrating that it is able to recover private client data from batches as large as 512, even under the presence of secure aggregation.

## 2 Related Work

In this section, we discuss prior work on gradient leakage attacks in federated learning.

**Honest server attacks** In the honest-but-curious setting, the existing attacks fall into three types. *Optimization-based attacks* [5, 21, 8, 9, 22, 10] optimize a dummy batch with SGD to match the user-provided gradient. *Analytical attacks* [6, 23] can recover inputs of linear layers in closed form, but are limited to batch size  $B = 1$  and do not support convolutional networks. *Recursive attacks* [7] extend analytical attacks to convolutional networks but are limited to  $B \leq 5$ . Several works thoroughly study these attacks [24, 25, 26, 11]. Crucially, Huang et al. [11] show that in realistic settings, where clients do not provide batchnorm statistics and labels, existing attacks are limited to  $B < 32$  for low-resolution data, and fail even for  $B = 1$  on high-resolution data. This implies that large  $B$  and secure aggregation [12] are effective in privacy protection against honest attacks.

**Malicious server (MS) attacks** As discussed above, we focus on the broadly applicable classes of boosted analytical [13, 14, 15, 16] and example disaggregation MS attacks [18, 17], elaborated

on in Sec. 3. Here, we reflect on other MS attacks that study more specific or orthogonal settings. Some works [14, 17] require the additional ability to send different updates to different users, which was shown easy to overcome with reverse aggregation [17]. The attack of Lam et al. [27] focuses on the rare setting where participation side-channel data is present. While we focus on images, various attacks consider other modalities, such as text [28, 29, 19, 20] or tabular data [30, 31]. Similarly, we consider only the threat of data reconstruction—some works [17] study important but strictly weaker privacy notions such as membership [32] or property inference [33]. Finally, another direction orthogonal to our work concerns the notably stronger threat model of sybil-based attacks [34, 35].

### 3 Detectability of Existing Malicious Server Attacks

As discussed in Sec. 1, most existing MS attacks are based on one of two key underlying principles, defining attack classes we term *boosted analytical* and *example disaggregation*. We now thoroughly discuss the issue of client-side detectability of those two attack classes, demonstrating that both are detectable using principled sanity checks. We point out the underlying reasons for this and formulate key desiderata that future attacks should satisfy to be more practically viable.

**Boosted analytical attacks** The work of Fowl et al. [13], Zhao et al. [14], Boenisch et al. [15], and Zhang et al. [16] uses model modifications to induce different variants of sparsity in dense layer gradients, enabling the application of honest analytical attacks to batch sizes beyond one. However, applying them to the realistic case of convolutional networks requires highly unusual *architectural modifications*, i.e., placing a large dense layer in front, which makes the attack obvious. The only alternative way to apply these attacks requires setting all convolutions to identity, such that the inputs are transmitted unchanged to the dense layer. As this is a pathological case that never occurs naturally and requires handcrafted changes to almost all parameters (e.g., 98% of ResNet18), this approach is easily detectable by inspecting model weights (e.g., by searching for convolutional filters with a single nonzero entry, see App. A). More importantly, it was shown [13] that meaningful levels of transmission are, in fact, not possible in realistic deep networks (due to pooling and strides), which future attempts to conceal the weight changes (e.g., by adding noise) would additionally worsen.

**Example disaggregation attacks** While the detectability of boosted analytical attacks was recognized in prior work [8, 15, 18], example disaggregation attacks [18, 17], proposed by Wen et al. [18], were thought to be more promising. These attacks use malicious model modifications to restrict the gradient flow for all examples but one, effectively causing the aggregated gradient of a large batch to be equal to the gradient of a single example. This undoes the protection of aggregation and allows the application of honest optimization-based attacks to reconstruct that example. While most instantiations of example disaggregation attacks rely on unusual handcrafted parameter changes, which are detectable in the *weight space* (same as for boosted analytical attacks), it may be possible to design variants that better disguise the restriction of the gradient flow. For this reason, we focus on a more fundamental limitation of all (current and future) example disaggregation attacks and demonstrate that they are always detectable in the *gradient space*. Moreover, such detection is possible without running costly optimization-based attacks by using a simple principled metric.

We now propose one such metric, the *disaggregation signal-to-noise ratio (D-SNR)*. Assuming the use of the standard cross-entropy loss  $\mathcal{L}(x, y)$ , a shared model with parameters  $\theta$ , and a batch of data  $D = \{(x_1, y_1), \dots, (x_B, y_B)\}$ , we define D-SNR as follows:

$$D\text{-SNR}(\theta, D) = \max_{W \in \theta_{lw}} \frac{\max_{i \in \{1, \dots, B\}} \left\| \frac{\partial \mathcal{L}(x_i, y_i)}{\partial W} \right\|}{\sum_{i=1}^B \left\| \frac{\partial \mathcal{L}(x_i, y_i)}{\partial W} \right\| - \max_{i \in \{1, \dots, B\}} \left\| \frac{\partial \mathcal{L}(x_i, y_i)}{\partial W} \right\|} \quad (1)$$

where  $\theta_{lw}$  denotes the set of weights of all linear layers (dense and convolutional; 98% of ResNet18 parameters). Intuitively, D-SNR searches for layers where the batch gradient (the average of example gradients) is dominated by the gradient of a single example, suggesting disaggregation. We conservatively use max to avoid false negatives and account for future attempts at partial disaggregation, i.e., if there is *any* layer that disaggregates a single point, then D-SNR will be large, and the client may decide to consider the batch vulnerable and skip the current round of training. While we focus on the case of disaggregating a single point, our approach can be easily generalized.

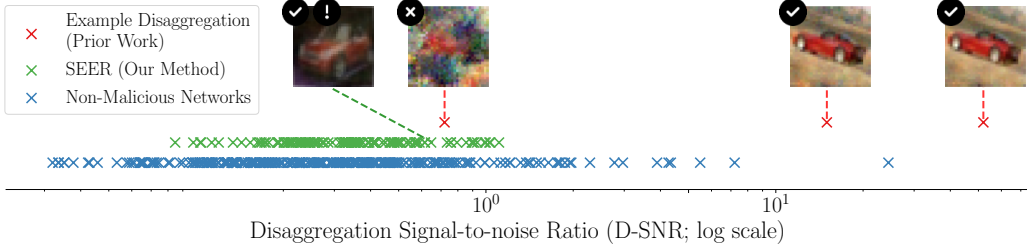


Figure 1: D-SNR (Sec. 3) of real (model, data batch) pairs. High values indicate vulnerability to data leakage, which can manifest even in non-malicious models (blue  $\times$ ). Example disaggregation attacks (red  $\times$ ) are easily detectable as they can successfully reconstruct data (green  $\checkmark$ ) only when D-SNR is unusually high (note the log scale), and fail otherwise (red  $\times$ ). Our method, SEER (green  $\times$ , Sec. 4), successfully reconstructs a datapoint even when D-SNR is low (green  $\checkmark$   $\ddagger$ ), and is thus hard to detect in the original gradient space.

We use D-SNR to experimentally study the detectability of example disaggregation attacks in realistic settings (see App. A for experimental details). As D-SNR is always  $\infty$  for attacks proposed by Wen et al. [18], we modify them in an attempt to smoothly control the strength of gradient flow restriction. Our key observation, presented in Fig. 1 (red  $\times$ ), is that in all cases where the attack is successful, D-SNR is unusually large, making the attack easily detectable. Reducing the strength of the gradient flow restriction further causes a sharp drop in D-SNR, entering the range of most non-malicious networks (blue  $\times$ ), i.e., the attack is undetectable. However, in all such cases, the attack fails, as the aggregation protects the examples. In rare cases (e.g., when overfitting), even natural networks can produce high D-SNR and be flagged. This behavior is *desirable*, as such networks indeed disaggregate a single example, and are thus (unintentionally) exposing sensitive user data. Thus, metrics such as D-SNR should be interpreted as detecting *vulnerability*, and not necessarily *maliciousness*.

**Desiderata for future attacks** Our results show that all prior MS attacks are client-side detectable with general checks. We argue that this is caused by fundamental problems of the two attack classes once their principles are known, and can not be remedied by further refinements. Any attempt to lift an honest analytical attack will inherit the limitation of being inapplicable to convolutions and will require architectural changes or handcrafted modifications detectable in the weight space. Lifting optimization-based attacks always requires example disaggregation, which is gradient space detectable. More broadly, as all information needed to execute these attacks is in the user gradients, the server has no informational advantage and no principled way to conceal the malicious intent.

This poses the question of finding novel attack principles that better exploit the potential of the MS threat model. To guide this and avoid common pitfalls, we now specify our threat model of interest and state several desiderata for future MS attacks guided by our results above, and observations from prior work [18, 11]. We argue that realistic MS data stealing attacks for image classification should: (i) target realistic deep convolutional networks and large batch sizes and/or secure aggregation; (ii) only utilize the attack vector of weight modifications, with no protocol changes (e.g., non-standard architectures, asymmetric client treatment) and no sybil capabilities; (iii) not assume unrealistic side information (e.g., batch normalization statistics or label information [11]); and (iv) explicitly consider the aspects of weight and gradient space detection (e.g., avoid obvious handcrafted modifications).

## 4 SEER: Data Stealing via Secret Embedding and Reconstruction

As a first step towards achieving the goals listed in Sec. 3, we propose *Data Stealing via Secret Embedding and Reconstruction* (SEER), a novel attack framework that steals data from large batch sizes while satisfying the above desiderata. SEER does not lift honest attacks and avoids straightforward gradient space detection by disaggregating the data in a hidden space defined by a server-side *secret decoder*. In Fig. 1, we see that SEER-trained networks (green  $\times$ ) have D-SNR values indistinguishable from those of natural networks. We do not use any handcrafted modifications and instead fine-tune the shared model and the secret modules with SGD, evading obvious weight space detection. The effectiveness of SEER in reconstructing user data is demonstrated in Sec. 5.

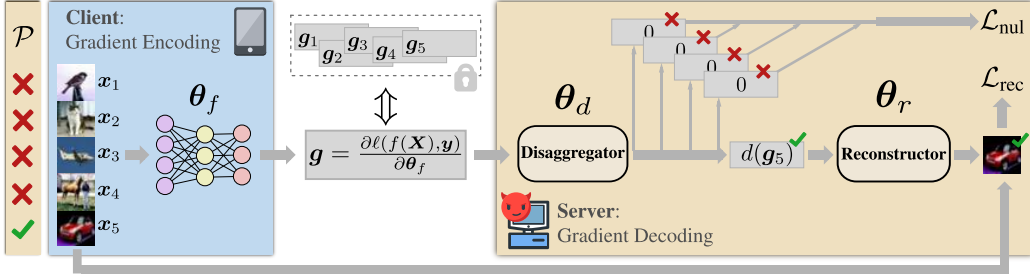


Figure 2: Overview of SEER. A client propagates a batch  $\mathbf{X}$  (of which one image satisfies the property  $\mathcal{P}$  only known to the server) through the shared network  $f$  with maliciously trained weights  $\theta_f$ , and returns the aggregated gradient  $\mathbf{g}$ , hoping that the aggregation protects individual images. The server steals the image that satisfies  $\mathcal{P}$  by applying a secret disaggregator  $d$  to remove the impact of other images in a hidden space, followed by a secret reconstructor  $r$ . SEER is trained by jointly optimizing  $\theta_f$ ,  $\theta_d$ , and  $\theta_r$  to minimize a combination of  $\mathcal{L}_{\text{nul}}$  and  $\mathcal{L}_{\text{rec}}$ .

**Mounting SEER** We first describe the stealing of data with SEER once trained (Fig. 2). Following usual FL protocols (for simplicity, we assume the FedSGD update rule), the client propagates their batch  $(\mathbf{X}, \mathbf{y})$  of  $B$  examples  $(\mathbf{x}_i, y_i)$  through the shared model  $f$  with parameters  $\theta_f$  sent by the server, and returns the gradient  $\mathbf{g} = \frac{\partial \ell(f(\mathbf{X}), \mathbf{y})}{\partial \theta_f}$  of the public loss  $\ell$ . Due to aggregation provided by large  $B$ ,  $\mathbf{g}$  is a mixture of gradients  $\mathbf{g}_i$  of individual examples, i.e.,  $\mathbf{g} = (1/B) \sum_{i=1}^B \mathbf{g}_i$ . In the case of secure aggregation, this also includes the gradients of other clients—we discuss this case shortly.

The server’s goal is to break this aggregation. To this end, the server passes  $\mathbf{g}$  through a previously trained *secret decoder*, consisting of a *disaggregator*  $d$  and a *reconstructor*  $r$ . If trained successfully, this computation reconstructs a single client image. The key mechanism of SEER that enables this is the idea of a *secret property*  $\mathcal{P}$  (far left in Fig. 2), which the server picks before training, keeps secret, and uses as a tool for disaggregation. While the exact choice of  $\mathcal{P}$  is not essential, the goal is to pick a property such that, as often as possible, *only one example in the batch satisfies it*. In Fig. 2, we set  $\mathcal{P}$  = “the least bright image in the batch” and observe (far left) that only  $\mathbf{x}_5$  satisfies it.

Crucially, if SEER is well optimized during training, the disaggregator  $d$  will map the aggregated gradient  $\mathbf{g}$  to a hidden space in which the projections of all images that do not satisfy  $\mathcal{P}$  are (approximately) removed, leaving only the projection of the target image (in our example,  $d(\mathbf{g}_5)$ ). This allows the reconstructor  $r$  to steal a single client image  $\mathbf{x}_5$ , shown on the far right.

**Training SEER** The trainable parameters of SEER, i.e.,  $\theta_f$ ,  $\theta_d$ , and  $\theta_r$ , can be interpreted as an encoder-decoder framework. After choosing the appropriate  $\mathcal{P}$ , the server performs end-to-end optimization of all components, using auxiliary data to simulate a real client. The goal of training is for  $d$  to nullify the contributions of images not satisfying  $\mathcal{P}$  (reflected by  $\mathcal{L}_{\text{nul}}$  in Fig. 2), and for  $r$  to reconstruct the image that satisfies  $\mathcal{P}$  from the output of  $d$  (reflected by  $\mathcal{L}_{\text{rec}}$ ). The weights of the shared model  $f$  are simultaneously fine-tuned to encode user data in the gradient space in a way that supports the goals of disaggregation and reconstruction. SEER does not utilize handcrafted weight changes of  $\theta_f$  and does not attempt to disaggregate the batch in the original space, avoiding both pitfalls of prior MS attacks that led to weight-space and gradient-space detectability.

#### 4.1 Key Components of SEER

We next describe the main components of SEER in more detail.

**Choosing properties** As noted above, before training, the server chooses a secret property  $\mathcal{P}$ , such that one image in each batch satisfies it. Let  $I_{\text{nul}} \subseteq [B] := \{1, \dots, B\}$  denote examples that do not satisfy  $\mathcal{P}$ , and  $I_{\text{rec}} \subseteq [B]$  those that do. In our experiments, we use brightness, inspired by Fowl et al. [13], who define  $\mathcal{P}$  as a threshold on the *global* brightness distribution of the dataset, such that  $I_{\text{rec}}$  covers probability mass  $\frac{1}{B}$ . This maximizes  $P(|I_{\text{rec}}| = 1)$ , approaching  $\frac{1}{e} \approx 37\%$  as  $B \rightarrow \infty$  [18].

We extend this, making a novel observation that for batch normalization (BN, present in most convolutional networks), we can choose  $\mathcal{P}$  such that, empirically,  $|I_{\text{rec}}| = 1$  for *nearly all batches*, for  $B$  as large as 512. This significantly improves the above probabilistic solution, as it implies

that in most cases, a single FL round is sufficient to steal client data. This is possible as each BN layer normalizes the distribution of its input, intertwining the computational graphs of images in the batch which are otherwise independent. With this in mind, we define  $\mathcal{P}$  with respect to the *local* distribution, e.g., as the maximal brightness in the batch. We find that SEER can learn such  $\mathcal{P}$  when trained with auxiliary data, almost always singling out the brightest image at attack time.

We remark that the case of secure aggregation [12] is more challenging, and *not equivalent* to a single large batch from a single client, an aspect that was overlooked in prior work. To overcome this challenge, we design a more elaborate  $\mathcal{P}$  as a combination of local and global properties, returning to the probabilistic success rate with probability approaching  $\frac{1}{e}$ , as in prior work. In the following, we will continue to assume that  $|I_{\text{rec}}| = 1$ . We provide a detailed explanation of this change in App. B, and in our experiments in Sec. 5 evaluate both large batch and secure aggregation variants of SEER.

**Training  $\theta_f$  for suitable gradient space encodings** We hypothesize that training the shared model weights  $\theta_f$  along with the secret decoder is one of the main reasons for the success of *SEER*. Intuitively, we can interpret the client-side gradient computation as a latent space encoding of their data. As discussed in Sec. 2, the failures of honest attacks in challenging settings suggest that this encoding is often insufficient to reconstruct user data. Our key observation is that the MS threat model allows us to overcome this by *controlling the encoding* by fine-tuning  $\theta_f$ , which was impossible in the honest setting. In particular, we maliciously optimize  $\theta_f$  with SGD to allow recovery of a single example by other parts of our framework, despite the loss of information inherent to this encoding. While such optimization-based modifications with auxiliary data were considered in one prior work on MS attacks [16], this work still inherits the fundamental limitations of all boosted analytical attacks, requiring additional handcrafted modifications which, as discussed in Sec. 3, are easily weight-space detectable—an issue which SEER circumvents by design.

**Training  $\theta_d$  for secret disaggregation** The secret disaggregator  $d$  addresses the key limitation of example disaggregation attacks (discussed in Sec. 3), which disaggregate examples in the gradient space. In contrast,  $d$  embeds the gradients from  $\mathbf{g}$  into a lower-dimensional space  $\mathbb{R}^{n_d}$  using a secret linear map  $\theta_d$ , concealing the disaggregation in the original gradient space. The benefits of using such a linear map are twofold. First, the lower-dimensional space allows us to more easily drive the gradients of  $I_{\text{nul}}$  to 0, which happens when they are in or close to the null space of  $\theta_d$ . Second, the linear map commutes with gradient aggregation due to additivity. Combining the two properties ((i) and (ii) in Eq. 2) ideally allows us to retain only the chosen sample from the aggregated gradient  $\mathbf{g}$ :

$$d(\mathbf{g}) = d\left(\sum_{i=1}^B \mathbf{g}_i\right) \stackrel{(i)}{=} \sum_{i=1}^B d(\mathbf{g}_i) = \sum_{i \in I_{\text{nul}}} d(\mathbf{g}_i) + \sum_{i \in I_{\text{rec}}} d(\mathbf{g}_i) \stackrel{(ii)}{\approx} \sum_{i \in I_{\text{rec}}} d(\mathbf{g}_i). \quad (2)$$

To achieve this in practice,  $f$  and  $d$  should be set such that  $d(\mathbf{g}_i) \approx 0$  for all  $i \in I_{\text{nul}}$ , but  $d(\mathbf{g}_i) \neq 0$  for the single  $i \in I_{\text{rec}}$ . To this end, for  $\mathcal{P}$  chosen as discussed above, we define the following objective:

$$\mathcal{L}_{\text{nul}} = \sum_{i \in I_{\text{nul}}} \|d(\mathbf{g}_i)\|_2^2, \quad (3)$$

which SEER aims to minimize during training. To ensure that this does not also nullify the gradient of the example of interest in  $I_{\text{rec}}$ , we proceed to discuss our reconstructor.

**Training  $\theta_r$  for image reconstruction** The final component of SEER we discuss is the secret reconstructor  $r: \mathbb{R}^{n_d} \rightarrow \mathbb{R}^{n_r}$ , which receives  $d(\mathbf{g})$ , i.e., the (noisy) isolated embedding of the target image gradient, as seen in Eq. 2. The reconstructor aims to map  $d(\mathbf{g})$  back to the original image  $\mathbf{x}_{\text{rec}}$ , effectively stealing that example from the original batch, compromising client privacy. To this end, we define the following  $\ell_2$  reconstruction objective, which is at odds with  $\mathcal{L}_{\text{nul}}$ :

$$\mathcal{L}_{\text{rec}} = \|r(d(\mathbf{g}_{\text{rec}})) - \mathbf{x}_{\text{rec}}\|_2^2. \quad (4)$$

The final loss function of SEER weighs the two losses using a hyperparameter  $\alpha > 0$ :

$$\mathcal{L} = \mathcal{L}_{\text{rec}} + \alpha \cdot \mathcal{L}_{\text{nul}}. \quad (5)$$

As previously noted, all three key components of SEER are jointly trained to minimize  $\mathcal{L}$ .

## 4.2 End-to-end Attack Description & Discussion

---

**Algorithm 1** The training procedure of SEER

---

```

1: function TRAINSEER( $f, \ell, B, \mathcal{X}, \mathcal{Y}$ )
2:   Choose  $\mathcal{P}$ , initialize  $d$  and  $r$ 
3:   while not converged do
4:      $\mathbf{X}, \mathbf{y} \leftarrow \{\mathbf{x}_i, \mathbf{y}_i \sim (\mathcal{X}, \mathcal{Y}) \mid i \in [B]\}$ 
5:      $I_{\text{nul}}, I_{\text{rec}} \leftarrow \mathcal{P}(\mathbf{X}, \mathbf{y})$ 
6:      $\mathbf{X}_{\text{nul}}, \mathbf{y}_{\text{nul}} \leftarrow \mathbf{X}[I_{\text{nul}}], \mathbf{y}[I_{\text{nul}}]$ 
7:      $\mathbf{X}_{\text{rec}}, \mathbf{y}_{\text{rec}} \leftarrow \mathbf{X}[I_{\text{rec}}], \mathbf{y}[I_{\text{rec}}]$ 
8:      $\mathbf{g}_{\text{nul}}, \mathbf{g}_{\text{rec}} \leftarrow \text{BP}(f, \ell, \mathbf{X}_{\text{nul}}, \mathbf{X}_{\text{rec}}, \mathbf{y}_{\text{nul}}, \mathbf{y}_{\text{rec}})$ 
9:      $\mathcal{L}_{\text{nul}} \leftarrow \|d(\mathbf{g}_{\text{nul}})\|_2^2$   $\triangleright$  Eq. 3
10:     $\mathcal{L}_{\text{rec}} \leftarrow \|r(d(\mathbf{g}_{\text{rec}})) - \mathbf{X}_{\text{rec}}\|_2^2$   $\triangleright$  Eq. 4
11:     $\mathcal{L} \leftarrow \mathcal{L}_{\text{rec}} + \alpha \cdot \mathcal{L}_{\text{nul}}$   $\triangleright$  Eq. 5
12:     $\theta_m \leftarrow \theta_m - \gamma_m \cdot \frac{\partial \mathcal{L}}{\partial \theta_m}, \forall m \in \{f, d, r\}$ 
13:   end while
14:   return  $f, d, r$ 
15: function BP( $f, \ell, \mathbf{X}_{\text{nul}}, \mathbf{X}_{\text{rec}}, \mathbf{y}_{\text{nul}}, \mathbf{y}_{\text{rec}}$ )
16:    $[\mathbf{l}_{\text{nul}}; \mathbf{l}_{\text{rec}}] \leftarrow \ell(f([\mathbf{X}_{\text{nul}}; \mathbf{X}_{\text{rec}}]), [\mathbf{y}_{\text{nul}}; \mathbf{y}_{\text{rec}}])$ 
17:   return  $\frac{\partial \mathbf{l}_{\text{nul}}}{\partial \theta_f}, \frac{\partial \mathbf{l}_{\text{rec}}}{\partial \theta_f}$ 

```

---

**Discussion** We now reflect on the desiderata listed in Sec. 3 and discuss how SEER fulfills them. First, SEER does not utilize any attack vector apart from maliciously modifying the weights of  $f$ , does not assume unrealistic knowledge of BN statistics or batch labels, and makes no assumptions regarding the label distributions, which is in contrast with some prior work [10, 18].

We remark that the necessity of such side information is the artifact of optimization-based attacks, and another reason why approaches that do not attempt to lift honest attacks (such as SEER) may be more promising. As noted above, SEER was greatly influenced by the assumption that clients *will* inspect the models, aiming to detect malicious updates. Namely, SEER avoids weight-space detectable handcrafted modifications and introduces secret disaggregation as means to avoid gradient-space detection. As shown in Sec. 5, SEER successfully steals client data on realistic convolutional networks with large batch sizes and secure aggregation, demonstrating its practicality.

## 5 Experimental Evaluation

In this section, we present our main experimental results, demonstrating that SEER is effective at reconstructing images from large batches of data on realistic networks, in both single-client and secure aggregation settings. The results of SEER are especially valuable given important advantages over prior work in terms of satisfying our desiderata from Sec. 3, as we discussed in Sec. 4.

**Experimental setup** We use ResNet18 [36] for all our experiments and consider 3 datasets—CIFAR10, for our main experiments, and CIFAR100 [37] and Restricted ImageNet (*ResImageNet*) [38], a subset of ImageNet [39] with 9 superclasses, to demonstrate our ability to scale with the number of labels and input size, respectively. In all experiments, we use the training set as our auxiliary data, and mount the attack on randomly sampled client batches of size  $B$  from the test (resp. validation) set for CIFAR10/100 (resp. ResImageNet). In App. C.1, we demonstrate SEER is robust to the client batch size  $B$  at attack time. We run all experiments on a single NVIDIA A100 GPU with 40GB and 80GB of VRAM for CIFAR10/100 and ResImageNet, respectively. Each CIFAR experiment took  $< 3$  GPU days to train and  $< 1$ h to mount the attack on 1000 batches. ResImageNet model trained for 11 GPU days, with an additional 0.5h to mount the attack on 100 batches. In the CIFAR experiments, as we observe that linear  $r$  performs well, we set  $r$  to a single linear layer and subsume  $d$  in it. For ResImageNet, we use a linear version of the U-Net decoder [40] (see App. D) to

Algorithm 1 describes the training of SEER. We train on client-sized batches (see Sec. 5 for a related study) sampled from our auxiliary data (Line 4). Based on  $\mathcal{P}$ , we select the index sets  $I_{\text{nul}}$  and  $I_{\text{rec}}$  (Line 5), representing the examples we aim to aggregate. Then, we simulate the client updates  $\mathbf{g}_{\text{rec}}$  and  $\mathbf{g}_{\text{nul}}$  computed on the full batch  $\mathbf{X}$  (Line 8), and use them to compute our optimization objective (Line 11). We minimize the objective by jointly training  $f$ ,  $d$ , and  $r$  using SGD (Line 12).

Mounting SEER once the malicious weights  $\theta_f$  have been trained using Algorithm 1 is simple, as we illustrate in Algorithm 2. The server, during an FL round, sends the client the malicious model  $f$  (Line 2), and receives the gradient update  $\mathbf{g}$ . Then, it applies its secret disaggregator  $d$  and reconstructor  $r$  (Line 3) to obtain  $\mathbf{x}_{\text{stolen}}$ , the reconstructed private example from the client batch.

---

**Algorithm 2** Mounting SEER

---

```

1: function MOUNTSEER( $f, d, r$ )
2:    $\mathbf{g} \leftarrow \text{GETCLIENTUPDATE}(f)$ 
3:    $\mathbf{x}_{\text{stolen}} \leftarrow r(d(\mathbf{g}))$ 
4:   return  $\mathbf{x}_{\text{stolen}}$ 

```

---

Table 1: Single-client reconstruction on bright and dark properties from batches of different sizes  $B$ . We report the percentage of well-reconstructed images ( $Rec$ ), the average PSNR and its standard deviation across all reconstructions ( $PSNR\ All$ ), and across the top 37% images ( $PSNR\ Top$ ). The other two settings (CIFAR100, Dark and CIFAR10, Bright) are deferred to App. C.2.

$B$	CIFAR10, Bright			CIFAR100, Dark		
	Rec (%)	PSNR Top	PSNR All	Rec (%)	PSNR Top	PSNR All
64	89.4	<b><math>32.1 \pm 2.0</math></b>	$27.2 \pm 5.3$	<b>97.0</b>	$32.8 \pm 1.3$	$29.3 \pm 4.1$
128	<b>94.2</b>	$31.9 \pm 1.7$	<b><math>28.2 \pm 4.3</math></b>	95.9	$30.5 \pm 1.3$	$26.8 \pm 3.8$
256	81.3	$29.0 \pm 2.1$	$24.4 \pm 4.9$	83.3	$25.7 \pm 1.3$	$22.2 \pm 3.4$
512	87.8	$26.6 \pm 1.8$	$23.2 \pm 3.5$	62.8	$24.3 \pm 1.5$	$20.2 \pm 4.0$

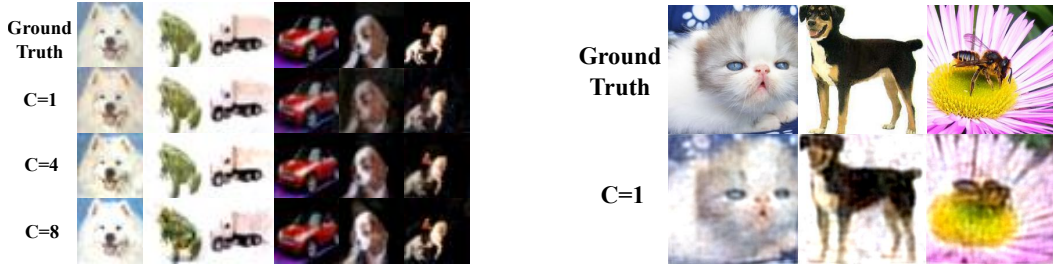


Figure 3: Example reconstructions of SEER with 128 total examples and different number of clients  $C$  on CIFAR10 (Left) and 64 examples on ResImageNet (Right).

allow better reconstruction quality and memory scaling. We defer additional information about our setup to App. E and App. F.

**Properties and metrics** In all reported experiments, we use the properties of maximal and minimal brightness (*Bright* and *Dark*), training a separate set of malicious weights for each (dataset, property, batch size) triple. We report 3 different metrics that describe our reconstruction quality. First, the percentage of reconstructed batches ( $Rec$ ), which represents the fraction of images with  $PSNR > 19$  [41] to the ground truth, which we consider satisfactory reconstruction. Second, we report the average PSNR across all attacked client batches. Finally, we report the average PSNR for the top  $\frac{1}{e} \approx 37\%$  of the batch reconstructions, allowing us to compare our single and multi-batch settings. We report our main results with other metrics in App. G. Next, we discuss our results.

**Single-batch reconstruction on CIFAR10/100** A reduced version of our main results is given in Table 1; the full results are deferred to App. C.2 and follow similar trends. We make several key observations. First, in most experiments, our local property allows us to reconstruct a large percentage of the batches (up to 97%), which is much higher than the theoretical limit  $\frac{1}{e}$  of probabilistic disaggregation, used in prior work. Second, we see that our reconstruction is independent of the property used and works well for both dark and bright images. Further, despite observing the expected trend that the quality of reconstruction degrades with the increased batch size  $B$ , our attack works well for a wide range of batch sizes and reconstructs up to 87.8% percent on images, even from batch sizes as large as 512. Third, we compare the results on the CIFAR10 and CIFAR100 datasets and notice no discernible difference in performance except for our  $B = 512$  experiments, where CIFAR10 is better. This suggests that for batch sizes where SEER obtains good results, the number of labels does not have a significant impact, but as the quality starts to degrade, it becomes a more significant factor. On top of the quantitative results, we also show example reconstructions of SEER in Fig. 3 (left,  $C = 1$ ), visually confirming the high quality of our reconstructions.

**Single-batch reconstruction on ResImageNet** To demonstrate that SEER scales to high-resolution images, we provide experiments on ResImageNet, chosen in order to eliminate our slight dependency on the number of classes, outlined above, and focus purely on the image size of the reconstructed inputs. We train a single model on  $B = 64$  with the bright property. Due to the computational demands of this experiment, caused by the very expensive forward passes of ImageNet images, we leave the full ablation study on different properties and batch sizes as a future work. To allow  $r$  and  $d$

Table 2: Multi-client reconstruction on the bright and dark properties using different number of clients  $C$  on CIFAR10, for different total numbers of points. We report the percentage of correctly reconstructed images (*Rec*) and the average PSNR across the top 37% images (*PSNR Top*).

#Pts	$C = 4$ , Dark		$C = 4$ , Bright		$C = 8$ , Dark		$C = 8$ , Bright	
	Rec (%)	PSNR Top	Rec (%)	PSNR Top	Rec (%)	PSNR Top	Rec (%)	PSNR Top
64	50.2	$27.5 \pm 3.0$	41.4	<b><math>27.3 \pm 3.1</math></b>	43.0	$27.4 \pm 3.3$	41.3	$26.6 \pm 3.7$
128	51.3	$28.8 \pm 2.6$	44.2	$26.8 \pm 3.0$	43.4	$27.6 \pm 3.5$	40.6	<b><math>27.3 \pm 3.3</math></b>
256	50.9	$29.8 \pm 2.3$	51.9	<b><math>27.3 \pm 2.5</math></b>	51.7	$27.0 \pm 2.9$	41.9	$25.4 \pm 3.1$
512	<b>61.3</b>	<b><math>30.2 \pm 2.4</math></b>	<b>52.9</b>	$25.7 \pm 2.4$	<b>56.3</b>	<b><math>28.7 \pm 2.9</math></b>	<b>51.7</b>	$25.9 \pm 2.8$

to scale to the output size of  $224 \times 224$ , we rely on a U-Net-like architecture based on multiple layers of transposed convolution with upsampling (see App. D). To speed up convergence, we pretrain a part of the transposed convolution stack, alongside  $\theta_f$ , on CIFAR10 and used it as initialization.

We obtain average PSNR of  $20.6 \pm 3.7$  and  $23.8 \pm 1.4$  on all and the top 37% of the images, respectively, corresponding to 77% successfully attacked batches. We note that these results are significant, as reconstructing even a single ImageNet image is not possible with honest attacks without restrictive assumptions of BN statistics and label data [11]. Some of our reconstructions are shown in Fig. 3 (right), where we see that images are clearly recognizable and accurate in terms of object positions. We note that the main factor degrading quality is salt-and-pepper-like noise caused by the noise introduced in our disaggregation step. We see the results from Fig. 3 as an encouraging result for the general applicability of our method.

**Reconstruction with secure aggregation** Finally, we present the results of our experiments in the secure aggregation setting in Table 2 with  $C = 4$  and  $C = 8$  clients, with batch sizes such that the total number of datapoints is the same as in Table 1. Most importantly, as for single batch reconstruction, our attack consistently obtains image reconstructions with an average  $\text{PSNR} > 25$ , i.e., recovers most images almost perfectly. Compared to Table 1, the attack probability of reconstruction degrades with  $C$ , confirming our intuition (see Sec. 4) that secure aggregation provides additional protection in the presence of BN, compared to simply using large batches. Despite this, we observe that the obtained success probability is still substantially higher than  $\frac{1}{e}$ . We suspect this is due to the model learning a restricted version of our single-batch reconstruction per individual client. We further compare the secure aggregation and single-batch variants of SEER in App. H.

Even more surprisingly, we notice that both reconstruction quality and the percentage of batches reconstructed rise with the number of aggregated points. Experimentally, for smaller batch sizes, we observe that this is caused by sampling too many images above the threshold defined by  $\mathcal{P}$  and thus failing to disaggregate as often. We believe that the observed improvement comes from a better estimation of the threshold on additional samples contained in larger batches. Finally, in Fig. 3 (left), we visually compare reconstructions in the single and multi-client settings, observing no noticeable degradation, which confirms that SEER is effective even in settings that use secure aggregation.

## 6 Outlook

We now reflect on the societal impact of our work, discuss potential mitigations and limitations of SEER, and outline several ideas for future work which we consider promising.

While SEER is a powerful attack that can harm user privacy, potentially demonstrating disparate impact [18], we believe our work opens the door to a more principled investigation of defenses, as it illustrates that techniques such as secure aggregation are not as effective as previously thought. To mitigate attacks such as SEER, prior work has discussed differential privacy methods such as DPSGD [42], which in the global model is incompatible with the MS setting as it requires a trusted aggregator, and in the local model [43] is known to degrade utility [44]. Further, cryptographic techniques such as SMPC or FHE are applicable in theory, but still largely impractical [45].

Thus, we believe that principled client-side detection is the most promising way forward. While SEER avoids pitfalls of prior attacks, which made them easily detectable, and we see no clear ways to detect

it in its current form, more sophisticated detection techniques may be able to do so. We encourage such work and advocate for efficient and robust checks accompanied by categorical analyses of attack classes (such as in our work), as opposed to ad-hoc detection which attack refinements can easily adapt to. On the attack side, interesting future directions include applying SEER to other data modalities and model architectures, improving its computational costs, investigating its dependence on in-distribution data, and attempting to generalize reconstruction beyond a single property.

## 7 Conclusion

In this work, we explored the issue of client-side detectability of malicious server (MS) attacks in federated learning. We demonstrated that all prior attacks are detectable in a principled way, and proposed SEER, a novel attack strategy that by design avoids such detection while effectively stealing data despite aggregation. Our work highlights the importance of studying attack detectability and represents a promising first step towards MS attacks that compromise privacy in realistic settings.

## References

- [1] Brendan McMahan, Eider Moore, Daniel Ramage, Seth Hampson, and Blaise Agüera y Arcas. Communication-efficient learning of deep networks from decentralized data. In *AISTATS*, 2017.
- [2] Brendan McMahan and Daniel Ramage. Federated learning: Collaborative machine learning without centralized training data. In *Google Research Blog*. <https://ai.googleblog.com/2017/04/federated-learning-collaborative.html>.
- [3] Matthias Paulik, Matt Seigel, Henry Mason, Dominic Telaar, Joris Kluivers, Rogier C. van Dalen, Chi Wai Lau, Luke Carlson, Filip Granqvist, Chris Vandeveld, Sudeep Agarwal, Julien Freudiger, Andrew Byde, Abhishek Bhowmick, Gaurav Kapoor, Si Beaumont, Áine Cahill, Dominic Hughes, Omid Javidbakht, Fei Dong, Rehan Rishi, and Stanley Hung. Federated evaluation and tuning for on-device personalization: System design & applications. *arXiv*, 2021.
- [4] FedAI. Utilization of fate in risk management of credit in small and micro enterprises. <https://www.fedai.org/>.
- [5] Ligeng Zhu, Zhijian Liu, and Song Han. Deep leakage from gradients. In *NeurIPS*, 2019.
- [6] Le Trieu Phong, Yoshinori Aono, Takuya Hayashi, Lihua Wang, and Shiho Moriai. Privacy-preserving deep learning via additively homomorphic encryption. *IEEE Trans. Inf. Forensics Secur.*, (5), 2018.
- [7] Junyi Zhu and Matthew B. Blaschko. R-GAP: recursive gradient attack on privacy. In *ICLR*, 2021.
- [8] Jonas Geiping, Hartmut Bauermeister, Hannah Dröge, and Michael Moeller. Inverting gradients- how easy is it to break privacy in federated learning? *NeurIPS*, 2020.
- [9] Jiahui Geng, Yongli Mou, Feifei Li, Qing Li, Oya Beyan, Stefan Decker, and Chunming Rong. Towards general deep leakage in federated learning. *arXiv*, 2021.
- [10] Hongxu Yin, Arun Mallya, Arash Vahdat, Jose M. Alvarez, Jan Kautz, and Pavlo Molchanov. See through gradients: Image batch recovery via gradinversion. In *CVPR*, 2021.
- [11] Yangsibo Huang, Samyak Gupta, Zhao Song, Kai Li, and Sanjeev Arora. Evaluating gradient inversion attacks and defenses in federated learning. In *NeurIPS*, 2021.
- [12] Kallista A. Bonawitz, Vladimir Ivanov, Ben Kreuter, Antonio Marcedone, H. Brendan McMahan, Sarvar Patel, Daniel Ramage, Aaron Segal, and Karn Seth. Practical secure aggregation for federated learning on user-held data. *NIPS*, 2016.
- [13] Liam H. Fowl, Jonas Geiping, Wojciech Czaja, Micah Goldblum, and Tom Goldstein. Robbing the fed: Directly obtaining private data in federated learning with modified models. In *ICLR*, 2022.
- [14] Joshua C. Zhao, Atul Sharma, Ahmed Roushdy Elkordy, Yahya H. Ezzeldin, Salman Avestimehr, and Saurabh Bagchi. Secure aggregation in federated learning is not private: Leaking user data at large scale through model modification. *arXiv*, 2023.
- [15] Franziska Boenisch, Adam Dziedzic, Roei Schuster, Ali Shahin Shamsabadi, Ilia Shumailov, and Nicolas Papernot. When the curious abandon honesty: Federated learning is not private. *arXiv*, 2021.
- [16] Shuaishuai Zhang, Jie Huang, Zeping Zhang, and Chunyang Qi. Compromise privacy in large-batch federated learning via malicious model parameters. In *ICA3PP*, 2023.
- [17] Dario Pasquini, Danilo Francati, and Giuseppe Ateniese. Eluding secure aggregation in federated learning via model inconsistency. In *CCS*, 2022.
- [18] Yuxin Wen, Jonas Geiping, Liam Fowl, Micah Goldblum, and Tom Goldstein. Fishing for user data in large-batch federated learning via gradient magnification. In *ICML*, 2022.

- [19] Liam Fowl, Jonas Geiping, Steven Reich, Yuxin Wen, Wojtek Czaja, Micah Goldblum, and Tom Goldstein. Decepticons: Corrupted transformers breach privacy in federated learning for language models. *ICLR*, 2022.
- [20] Hong-Min Chu, Jonas Geiping, Liam H Fowl, Micah Goldblum, and Tom Goldstein. Panning for gold in federated learning: Targeted text extraction under arbitrarily large-scale aggregation. *ICLR*, 2023.
- [21] Bo Zhao, Konda Reddy Mopuri, and Hakan Bilen. idlg: Improved deep leakage from gradients. *arXiv*, 2020.
- [22] Ruihan Wu, Xiangyu Chen, Chuan Guo, and Kilian Q Weinberger. Learning to invert: Simple adaptive attacks for gradient inversion in federated learning. *arXiv*, 2021.
- [23] Sanjay Kariyappa, Chuan Guo, Kiwan Maeng, Wenjie Xiong, G. Edward Suh, Moinuddin K. Qureshi, and Hsien-Hsin S. Lee. Cocktail party attack: Breaking aggregation-based privacy in federated learning using independent component analysis. *arXiv*, 2022.
- [24] Kai Yue, Richeng Jin, Chau-Wai Wong, Dror Baron, and Huaiyu Dai. Gradient obfuscation gives a false sense of security in federated learning. *arXiv*, 2022.
- [25] Mislav Balunovic, Dimitar Iliev Dimitrov, Robin Staab, and Martin T. Vechev. Bayesian framework for gradient leakage. In *ICLR*, 2022.
- [26] Xiao Jin, Pin-Yu Chen, Chia-Yi Hsu, Chia-Mu Yu, and Tianyi Chen. CAFE: catastrophic data leakage in vertical federated learning. *arXiv*, 2021.
- [27] Maximilian Lam, Gu-Yeon Wei, David Brooks, Vijay Janapa Reddi, and Michael Mitzenmacher. Gradient disaggregation: Breaking privacy in federated learning by reconstructing the user participant matrix. In *ICML*, 2021.
- [28] Mislav Balunovic, Dimitar I. Dimitrov, Nikola Jovanovic, and Martin T. Vechev. LAMP: extracting text from gradients with language model priors. In *NeurIPS*, 2022.
- [29] Samyak Gupta, Yangsibo Huang, Zexuan Zhong, Tianyu Gao, Kai Li, and Danqi Chen. Recovering private text in federated learning of language models. In *NeurIPS*, 2022.
- [30] Han Wu, Zilong Zhao, Lydia Y. Chen, and Aad van Moorsel. Federated learning for tabular data: Exploring potential risk to privacy. In *ISSRE*, 2022.
- [31] Mark Vero, Mislav Balunovic, Dimitar I. Dimitrov, and Martin T. Vechev. Data leakage in tabular federated learning. *ICML*, 2022.
- [32] Jiayuan Ye, Aadyaa Maddi, Sasi Kumar Murakonda, Vincent Bindschaedler, and Reza Shokri. Enhanced membership inference attacks against machine learning models. In *CCS*, 2022.
- [33] Luca Melis, Congzheng Song, Emiliano De Cristofaro, and Vitaly Shmatikov. Exploiting unintended feature leakage in collaborative learning. In *IEEE Symposium on Security and Privacy*, 2019.
- [34] Clement Fung, Chris J. M. Yoon, and Ivan Beschastnikh. The limitations of federated learning in sybil settings. In *RAID*, 2020.
- [35] Franziska Boenisch, Adam Dziedzic, Roei Schuster, Ali Shahin Shamsabadi, Ilia Shumailov, and Nicolas Papernot. Reconstructing individual data points in federated learning hardened with differential privacy and secure aggregation. *arXiv*, 2023.
- [36] Kaiming He, Xiangyu Zhang, Shaoqing Ren, and Jian Sun. Deep residual learning for image recognition. In *Proceedings of the IEEE conference on computer vision and pattern recognition*, pages 770–778, 2016.
- [37] Alex Krizhevsky, Geoffrey Hinton, et al. Learning multiple layers of features from tiny images. 2009.

- [38] Dimitris Tsipras, Shibani Santurkar, Logan Engstrom, Alexander Turner, and Aleksander Madry. Robustness may be at odds with accuracy. *arXiv preprint arXiv:1805.12152*, 2018.
- [39] Jia Deng, Wei Dong, Richard Socher, Li-Jia Li, Kai Li, and Li Fei-Fei. Imagenet: A large-scale hierarchical image database. In *2009 IEEE conference on computer vision and pattern recognition*, pages 248–255. Ieee, 2009.
- [40] Olaf Ronneberger, Philipp Fischer, and Thomas Brox. U-net: Convolutional networks for biomedical image segmentation. In *Medical Image Computing and Computer-Assisted Intervention–MICCAI 2015: 18th International Conference, Munich, Germany, October 5–9, 2015, Proceedings, Part III 18*, pages 234–241. Springer, 2015.
- [41] Alain Horé and Djemel Ziou. Image quality metrics: Psnr vs. ssim. In *2010 20th International Conference on Pattern Recognition*, pages 2366–2369, 2010. doi: 10.1109/ICPR.2010.579.
- [42] Martín Abadi, Andy Chu, Ian J. Goodfellow, H. Brendan McMahan, Ilya Mironov, Kunal Talwar, and Li Zhang. Deep learning with differential privacy. In *CCS*, 2016.
- [43] Stacey Truex, Ling Liu, Ka Ho Chow, Mehmet Emre Gursoy, and Wenqi Wei. Ldp-fed: federated learning with local differential privacy. In *EdgeSys@EuroSys*, 2020.
- [44] Kang Wei, Jun Li, Ming Ding, Chuan Ma, Howard H. Yang, Farhad Farokhi, Shi Jin, Tony Q. S. Quek, and H. Vincent Poor. Federated learning with differential privacy: Algorithms and performance analysis. *arXiv*, 2019.
- [45] Peter Kairouz, H. Brendan McMahan, Brendan Avent, Aurélien Bellet, Mehdi Bennis, Arjun Nitin Bhagoji, Kallista A. Bonawitz, Zachary Charles, Graham Cormode, Rachel Cummings, Rafael G. L. D’Oliveira, Salim El Rouayheb, David Evans, Josh Gardner, Zachary Garrett, Adrià Gascón, Badih Ghazi, Phillip B. Gibbons, Marco Gruteser, Zaïd Harchaoui, Chaoyang He, Lie He, Zhouyuan Huo, Ben Hutchinson, Justin Hsu, Martin Jaggi, Tara Javidi, Gauri Joshi, Mikhail Khodak, Jakub Konečný, Aleksandra Korolova, Farinaz Koushanfar, Sanmi Koyejo, Tancrède Lepoint, Yang Liu, Prateek Mittal, Mehryar Mohri, Richard Nock, Ayfer Özgür, Rasmus Pagh, Mariana Raykova, Hang Qi, Daniel Ramage, Ramesh Raskar, Dawn Song, Weikang Song, Sebastian U. Stich, Ziteng Sun, Ananda Theertha Suresh, Florian Tramèr, Praneeth Vepakomma, Jianyu Wang, Li Xiong, Zheng Xu, Qiang Yang, Felix X. Yu, Han Yu, and Sen Zhao. Advances and open problems in federated learning. *arXiv*, 2019.

# Supplementary Material

## A Detectability Experiments

Here we provide more details regarding our detectability experiments.

**Measuring D-SNR** To produce Fig. 1, we consider 4 SEER-trained malicious models (CIFAR10, *Bright/Dark*, batch size 128/256), as well as 8 checkpoints made at various points during natural training, using the same initialization as used for SEER. Then, for each value of  $B \in \{16, 32, 64\}$ , we choose 5 random batches of size  $B$  from the training set and 5 random batches of size  $B$  from the test set of CIFAR10. For each batch, we compute the D-SNR on each of the 12 networks using Eq. 1 and plot the resulting value as a point in Fig. 1 (blue for natural and green for SEER networks). For example disaggregation attacks, we use a publicly available implementation of the attacks of [18] and modify the *multiplier* parameter to control the strength of the attack. We use the default setting where batches are chosen such that all images belong to the same class (*car* in this case). The three reconstructions of the example disaggregation attack are obtained by running the modernized variant of the attack of Geiping et al. [8] on the disaggregated batch. The modernized variant is implemented in the Breaching framework, which Wen et al. [18] is a part of. Finally, for the reconstruction of SEER, we aimed to show an image from the same class (a car), with D-SNR slightly below the D-SNR of the leftmost example disaggregation point (0.72). To do this, we use the *Dark* property and the dark car image from Fig. 3, and sample the other 63 points in the batch randomly from the test set until the D-SNR falls in the [0.62, 0.72] range. We stop as soon as we find such a batch and report the reconstruction produced by SEER.

**Measuring transmission** As noted in Sec. 3, to be applicable to convolutional networks, boosted analytical attacks require handcrafted changes to convolutional layers that simply transmit the inputs unchanged. While, as noted above, even in the ideal case, this cannot lead to good reconstructions, we illustrate the point that such change is detectable by defining a metric similar to D-SNR, which can be interpreted as a *transmission signal-to-noise ratio*, measured on the first convolutional layer. Namely, for each filter in the first convolutional layer, we divide the absolute values of the largest entry by the sum of the absolute values of all other entries. Intuitively, we treat the entry with the largest absolute value as the signal, and measure how well this is transmitted by the filter. The ratio is high when the filter transmits the input unchanged, and is  $\infty$  for the handcrafted changes used by the boosted analytical attacks. We compute this metric on the 12 networks used in Fig. 1 (see previous paragraph) and show the results in Fig. 4. Intuitively, the red line at 1.0 indicates the case where there are equal amounts of the pixel being transmitted and all other pixels. We can observe that all networks have values below 0.3, confirming that transmission is indeed unusual and not a case that ever happens naturally, implying that if boosted analytical attacks that use this technique would be able to obtain good results, they would still be easily detectable in the weight space.

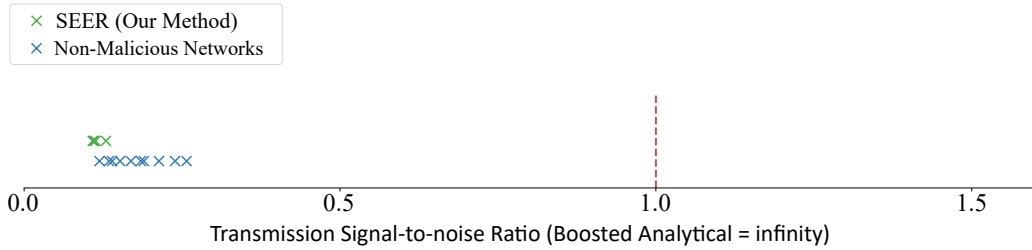


Figure 4: The transmission signal-to-noise ratio of several SEER-trained and naturally trained networks. The same metric has a value of  $\infty$  for all boosted analytical attacks.

Table 3: Single-client reconstruction on the bright property on CIFAR10 on a network trained with batch size  $B = 128$  and tested for various client batch sizes  $B_{\text{test}}$ . We report the percentage of well-reconstructed images ( $\text{Rec}$ ), the average PSNR and its standard deviation on all reconstructions ( $\text{PSNR All}$ ), and across the top 37% images ( $\text{PSNR Top}$ ).

$B_{\text{test}}$	Rec (%)	PSNR Top $\uparrow$	PSNR All $\uparrow$
64	42.0%	$21.51 \pm 1.83$	$18.51 \pm 2.93$
96	87.4%	$30.56 \pm 1.31$	$26.28 \pm 4.92$
128	<b>94.2%</b>	<b><math>31.91 \pm 1.73</math></b>	<b><math>28.15 \pm 4.34</math></b>
192	86.3%	$30.78 \pm 2.37$	$25.77 \pm 5.14$
256	67.5%	$28.02 \pm 2.79$	$22.42 \pm 5.14$

## B Reconstructing from Securely-Aggregated Gradient Updates

As described in Sec. 4.1, we have designed a more elaborate property  $\mathcal{P}$  for the case of attacking securely aggregated gradient updates. Our property is based on a combination of local (in-batch) and global distribution information about the client data allowing us to handle this more complex case. In this section, we describe in detail how this is done.

As described in Sec. 4.1, we need to define the property  $\mathcal{P}$  with respect to a range of brightnesses, such that  $P(|I_{\text{rec}}| = 1)$  is maximized. Thus, generating  $\mathcal{P}$  is reduced to finding the correct thresholds on the client image brightnesses, with which we later train SEER.

To calculate the threshold  $\tau$  in the multi-client setting, we use the insight that individual client batches are still generated in the presence of BN before their aggregation. To this end, we normalize the brightnesses within individual client batches of size  $B$  for 20000 sampled client batches and use the sampled normalized brightness to generate the cumulative density function(CDF) of their empirical distribution. We then choose the threshold  $\tau$  on this distribution to maximize the probability that exactly one out of the  $C$  aggregated clients has exactly one image with normalized brightness above the threshold. For simplicity, we demonstrate this in the case of maximal brightness, as the minimal-brightness case is equivalent. We estimate the probability of having exactly one image with normalized brightness above the threshold as:

$$(1 - \Phi_1(\tau)) * \Phi_2(\tau) * \Phi_1(\tau)^{C-1} \quad (6)$$

where  $\Phi_1$  is the CDF of the top brightness in a sampled batch, and  $\Phi_2$  is the CDF of the second-highest brightness in a sampled batch. The equation can be intuitively rephrased as follows—for exactly one client, the highest normalized brightness within its batch is above  $\tau$ , and the second-highest brightness is below  $\tau$ , while for the rest, all brightnesses are below  $\tau$ . To optimize Eq. 6 for the threshold  $\tau$ , we use the golden section search method - a numerical optimization technique that repeatedly divides a search interval by the golden ratio to efficiently locate the (possibly-local) extremum of a function of a single variable.

## C Additional Experiments

In this section, we provide additional experimental results, which we did not include in the main body due to space constraints.

### C.1 Robustness to $B$

In this section, we demonstrate that attack parameters  $\theta_f$  generated by SEER for a particular client batch size  $B$  can work to a large extent for batch sizes close to the original one, thus relaxing the requirement that the exact client batch size  $B$  is known during the crafting of the malicious model  $f$ . In particular, in Table 3, we show the effect of applying our single-client attack trained on  $B = 128$  on CIFAR10 using the *Bright* image property for clients with varying batch sizes  $B_{\text{test}}$ . We observe that while, as expected, SEER performs best when  $B_{\text{test}} = B$ , both the success rate and the quality of reconstruction on clients with batch sizes even  $2\times$  larger than the trained one remain very good. We note that Table 3 suggests that underestimating the client batch size  $B_{\text{test}}$  during the training of  $f$

Table 4: Single-client reconstruction on bright and dark properties from batches of different sizes  $B$  on CIFAR10. We report the percentage of well-reconstructed images ( $Rec$ ), the average PSNR and its standard deviation on all reconstructions ( $PSNR\ All$ ), and across the top 37% images ( $PSNR\ Top$ ).

$B$	CIFAR10, Dark			CIFAR10, Bright		
	Rec (%)	PSNR Top $\uparrow$	PSNR All $\uparrow$	Rec (%)	PSNR Top $\uparrow$	PSNR All $\uparrow$
64	82.0	<b><math>32.0 \pm 1.6</math></b>	<b><math>26.6 \pm 6.6</math></b>	89.4	<b><math>32.1 \pm 2.0</math></b>	$27.2 \pm 5.3$
128	74.5	$29.5 \pm 1.4$	$23.6 \pm 6.2$	<b>94.2</b>	$31.9 \pm 1.7$	<b><math>28.2 \pm 4.3</math></b>
256	67.6	$26.6 \pm 1.7$	$21.6 \pm 4.8$	81.3	$29.0 \pm 2.1$	$24.4 \pm 4.9$
512	<b>82.3</b>	$26.8 \pm 1.3$	$22.8 \pm 4.0$	87.8	$26.6 \pm 1.8$	$23.2 \pm 3.5$

Table 5: Single-client reconstruction on bright and dark properties from batches of different sizes  $B$  on CIFAR100. We report the percentage of well-reconstructed images ( $Rec$ ), the average PSNR and its standard deviation across all reconstructions ( $PSNR\ All$ ), and on the top 37% images ( $PSNR\ Top$ ).

$B$	CIFAR100, Dark			CIFAR100, Bright		
	Rec (%)	PSNR Top $\uparrow$	PSNR All $\uparrow$	Rec (%)	PSNR Top $\uparrow$	PSNR All $\uparrow$
64	<b>97.0</b>	<b><math>32.8 \pm 1.3</math></b>	<b><math>29.3 \pm 4.1</math></b>	<b>95.6</b>	<b><math>32.2 \pm 1.5</math></b>	<b><math>28.2 \pm 4.3</math></b>
128	95.9	$30.5 \pm 1.3$	$26.8 \pm 3.8$	94.7	$30.0 \pm 1.3$	$26.5 \pm 3.7$
256	83.3	$25.7 \pm 1.3$	$22.2 \pm 3.4$	82.2	$25.4 \pm 1.1$	$22.1 \pm 3.4$
512	62.8	$24.3 \pm 1.5$	$20.2 \pm 4.0$	38.4	$21.6 \pm 1.4$	$17.4 \pm 3.9$

is better than overestimating it, as the reconstruction performance when  $B_{\text{test}} = 64$  is significantly worse than when  $B_{\text{test}} = 256$ . This is mostly caused by  $d$  filtering out all images in the client batches resulting in the removal of all the client data.

## C.2 Extended Single Client Experiments

In Table 4 and Table 5, we present the extended version of our CIFAR10 and CIFAR100 single-client experiments, first presented in Sec. 5. We observe similar trends as in the original experiments. For example, we observe that CIFAR10 and CIFAR100 performances are similar up to  $B = 256$  and that there is no major difference in performance between the most bright and most dark image properties.

## D U-Net-based Image Reconstructor

In this section, we explain the architecture of our image reconstructor  $r$  used in our ResImageNet experiments in Sec. 5. Our architecture is inspired by the decoder portion of a U-Net [40], which has been demonstrated to be a memory-efficient architecture for generating images.

We show our architecture in Fig. 5. In the figure,  $g$  depicts our model’s gradient subsampled randomly so that only 3% of its entries are kept (See App. F.1). There are two main differences between our  $r$  in Fig. 5 and the original 6-layer U-Net architecture. First, we use no activation functions, thus creating a (sparse) linear reconstructor function  $r$ . This allows us, similarly to our CIFAR10/100 experiments, to combine  $r$  and  $d$  into a single linear layer, whose bias becomes the target for our filtered-out inputs  $X_{\text{nul}}$ . Second, as our architecture does not include U-Net-style encoder, the U-connections of our reconstructor are substituted by pairs of linear layers with a bottleneck in the middle applied on  $g$ . In Fig. 5, we depict the bottleneck sizes and transposed convolution sizes, as well as the intermediate output sizes of the different layers. The bottlenecks ensure that the memory efficiency of our method is preserved and are inspired by the intuition that the U-connections only need to provide high-frequency content which can live in a much lower-dimensional subspace. Finally, we note that for the purpose of pretraining, we used the first 3 channels of the third transposed convolution layer

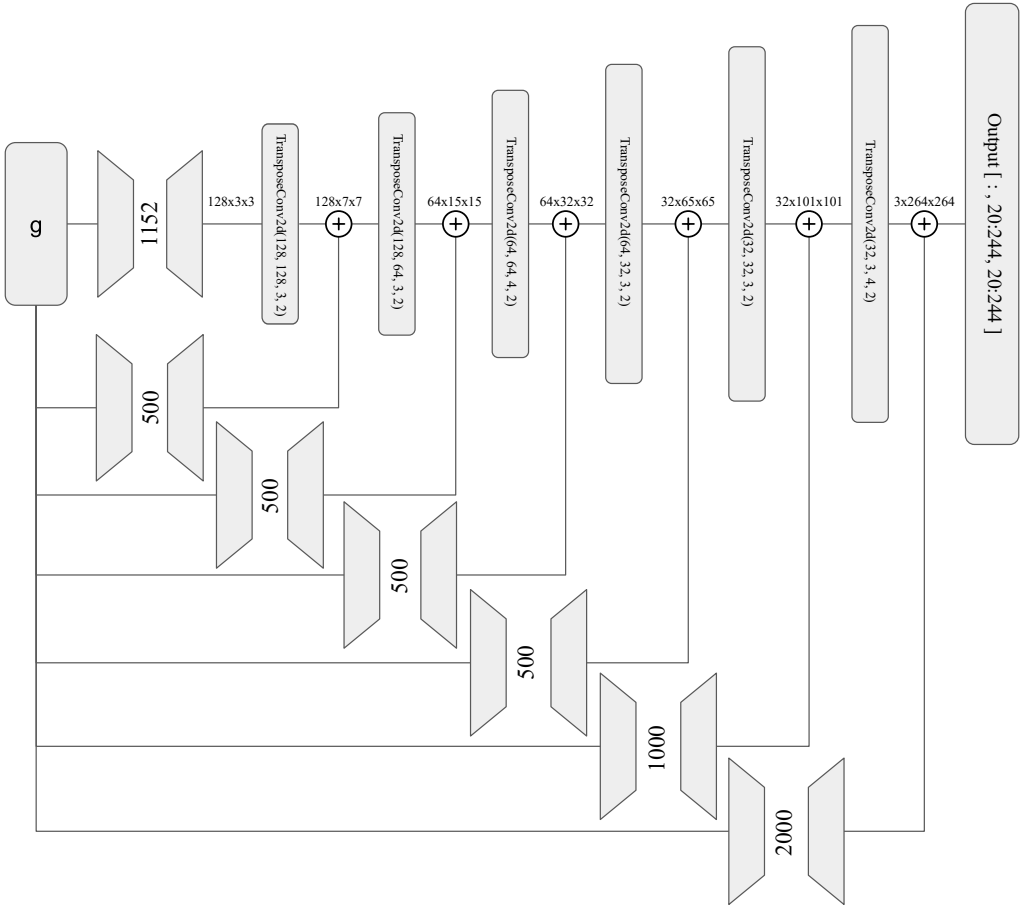


Figure 5: The architecture of our U-Net-based reconstructor  $r$  used in our ResImageNet experiments. Here  $g$  is the randomly subsampled model gradient and the output is the resulting reconstructed image.

as our CIFAR10 output and that our transposed convolution stack produces images of size  $264 \times 264$ , which we then center-crop to produce our ImageNet-sized final output.

## E Hyperparameters

In this section, we provide more details about the exact hyperparameters used in our experiments in Sec. 5. We implemented SEER in Pytorch 1.13. Throughout our experiments, we used the Adam optimizer with a learning rate of 0.0001. To stabilize our training convergence, we adopted gradient accumulation and, thus, updated our modules' parameters only once every 10 gradient steps. For CIFAR10/100, we trained between 500 and 1000 epochs, where an epoch is defined to be 1000 sampled batches from our trainset. Having gradient accumulation set to 10 amounts to 100 gradient descent steps per epoch. For ResImageNet, we trained for 370 epochs instead, with 400 gradient descent steps per epoch. For faster convergence and better balance in the optimized objective  $\mathcal{L} = \mathcal{L}_{\text{rec}} + \alpha \cdot \mathcal{L}_{\text{nul}}$ , we adopted a schedule for the hyperparameter  $\alpha$ , following an exponential curve of the epoch  $\kappa$ .

The schedule is defined as:  $\alpha(\kappa) = \min(|B|, 2^{\beta(\kappa)})$ , where  $\beta(\kappa) = \frac{(K-\kappa)\beta_0 + \kappa\beta_1}{K}$  linearly interpolates between  $\beta_0$  and  $\beta_1$  across the total number of epochs  $K$  with  $(\beta_0, \beta_1)$  set to  $(-2, \log_2|B|)$ . For ResImageNet, we set  $(\beta_0, \beta_1)$  to  $(-5, 5.3)$  to allow for better reconstruction earlier in the training process. Finally, we point out that in the multi-client setting, we estimate the cumulative density functions before training for the first and second-highest brightness in a batch on 20000 randomly sampled batches from the trainset (see App. B).

## F Implementation Details

### F.1 Subsampled gradients

In order to save memory and computation, we use only part of the entries in our full model gradient  $\mathbf{g}$  to construct our intermediate disaggregation space  $\mathbb{R}^{n_d}$ . In particular, we randomly sample 0.1% of the gradient entries of each of the model’s parameters while ensuring that at least 8400 entries per parameter are sampled for our CIFAR10/100 experiments, and 2% and at least 9800 entries for our ResImageNet experiments. This results in 1.6% of the total gradient entries for CIFAR10/100 and 3.0% for ResImageNet. We theorize that we are able to reconstruct nearly perfectly with such a small percent of the gradient entries because there is large redundancy in the information different gradient entries provide.

### F.2 Efficiently Computing the Disaggregation Loss $\mathcal{L}_{\text{nul}}$

Computing  $\mathcal{L}_{\text{nul}}$  directly for large batch sizes  $B$  takes a lot of memory due to the need to store  $\mathbf{g}_i$  for all  $i$  in the large set  $I_{\text{nul}}$ . Note that the reason for this is that we want to enforce all of the individual gradient  $\mathbf{g}_i$  to fall in the null space of  $\theta_d$  separately. In practice, to save space, we enforce the same condition by computing the surrogate:

$$\widehat{\mathcal{L}}_{\text{nul}} = \left\| \frac{1}{|I_{\text{nul}}|} \sum_{i \in I_{\text{nul}}} d(\mathbf{g}_i) \right\|_2^2 + \left\| d(\mathbf{g}_{j \sim I_{\text{nul}}}) \right\|_2^2,$$

where the first part of the equation enforces the mean gradient, and the second part enforces a different randomly chosen gradient at every SGD to both approach 0. This, in practice, has a similar result to the original loss  $\mathcal{L}_{\text{nul}}$  in that, over time, all gradients in  $I_{\text{nul}}$  go to 0.

### F.3 Trainset data augmentation

For the purpose of training our encoder-decoder framework, we observed data augmentation of our auxiliary dataset is crucial, especially for large batch sizes  $B$ . We theorize that the reason for this is the lack of diversity in the reconstruction samples  $\mathbf{X}_{\text{rec}}$ . In particular, as  $B$  grows, an increasingly smaller set of images are selected to be the brightest or darkest of any batch sampled from the training set. To this end, when sampling our training batches for CIFAR10/100, we first apply random ColorJitter with brightness, contrast, saturation, and hue parameters 0.2, 0.1, 0.1, and 0.05, respectively, followed by random horizontal and vertical flips, and random rotation at  $N * 90 + \epsilon$  degrees, where  $N$  is a random integer and  $\epsilon$  is chosen uniformly at random on  $[-5, 5]$ . For ResImageNet, we additionally do a random cropping of the original image to the desired size of  $224 \times 224$  before the other augmentations.

### F.4 Trainset batch augmentation

When dealing with multiple clients, as detailed in App. B, we adopt a probabilistic approach. As noted in Sec. 4.1, the probability of attack success with a perfect threshold  $\tau$  is  $\frac{1}{e}$  in the limit of the number of images being aggregated. As we need SEER to successfully reconstruct images only in the  $\frac{1}{e}$  fraction of the securely-aggregated batches, where we are expected to successfully disaggregate, we avoid training on the rest  $1 - \frac{1}{e} > \frac{1}{2}$  fraction of the securely-aggregated batches, which can act as a strong noise factor during training and prevent convergence. This, in turn, results in rejecting training on a big portion of our sampled client batches.

To address this sample inefficiency, we use batch augmentation during training to transform the client batches to ones with a desired brightness distribution. The batch augmentation simply consists of adjusting the brightnesses of individual images within each batch. We do two types of batch augmentations based on two different distributions—one where it contains precisely one image in the batch with brightness above the threshold  $\tau$  and another where precisely zero images in the batch have brightness above the threshold  $\tau$ . We alternate the two augmentations at each step of the training procedure. To achieve the distributions, we adjust all image brightness within a batch using a heuristic method. The method first adjusts the brightness of the most bright image (least bright image in the case of the dark image property) such that it lands on the desired side of the threshold  $\tau$ . However, as after adjusting the image, the brightnesses within the batch are no longer normalized, we then need to

Table 6: Single-client reconstruction on bright and dark properties from batches of different sizes  $B$  on CIFAR10. We report several additional quality of reconstruction metrics—the average MSE and its standard deviation across all reconstructions (*MSE All*), and on the top 37% images (*MSE Top*), as well as, the average LPIPS and its standard deviation across all reconstructions (*LPIPS All*), and on the top 37% images (*LPIPS Top*).

$B$	CIFAR10, Dark				CIFAR10, Bright			
	MSE Top ↓	MSE All ↓	LPIPS Top ↓	LPIPS All ↓	MSE Top ↓	MSE All ↓	LPIPS Top ↓	LPIPS All ↓
64	<b>0.0007 ± 0.0002</b>	0.0096 ± 0.0225	<b>0.058 ± 0.020</b>	<b>0.166 ± 0.180</b>	<b>0.0007 ± 0.0002</b>	0.0048 ± 0.0099	<b>0.046 ± 0.026</b>	<b>0.104 ± 0.099</b>
128	0.0012 ± 0.0004	0.0138 ± 0.0258	0.113 ± 0.027	0.240 ± 0.167	<b>0.0007 ± 0.0002</b>	<b>0.0031 ± 0.0060</b>	0.057 ± 0.025	<b>0.104 ± 0.081</b>
256	0.0023 ± 0.0008	0.0132 ± 0.0171	0.195 ± 0.046	0.302 ± 0.123	0.0014 ± 0.0005	0.0074 ± 0.0112	0.122 ± 0.046	0.200 ± 0.112
512	0.0022 ± 0.0006	<b>0.0086 ± 0.0113</b>	0.224 ± 0.049	0.306 ± 0.102	0.0024 ± 0.0007	0.0070 ± 0.0091	0.168 ± 0.058	0.204 ± 0.089

Table 7: Single-client reconstruction on bright and dark properties from batches of different sizes  $B$  on CIFAR100. We report several additional quality of reconstruction metrics—the average MSE and its standard deviation across all reconstructions (*MSE All*), and on the top 37% images (*MSE Top*), as well as, the average LPIPS and its standard deviation across all reconstructions (*LPIPS All*), and on the top 37% images (*LPIPS Top*).

$B$	CIFAR100, Dark				CIFAR100, Bright			
	MSE Top ↓	MSE All ↓	LPIPS Top ↓	LPIPS All ↓	MSE Top ↓	MSE All ↓	LPIPS Top ↓	LPIPS All ↓
64	<b>0.0005 ± 0.0001</b>	<b>0.0027 ± 0.0095</b>	<b>0.064 ± 0.021</b>	<b>0.105 ± 0.088</b>	<b>0.0006 ± 0.0002</b>	<b>0.0028 ± 0.0047</b>	<b>0.050 ± 0.023</b>	<b>0.094 ± 0.075</b>
128	0.0009 ± 0.0003	0.0033 ± 0.0044	0.125 ± 0.033	0.169 ± 0.068	0.0010 ± 0.0003	0.0035 ± 0.0045	0.112 ± 0.035	0.164 ± 0.076
256	0.0028 ± 0.0008	0.0088 ± 0.0112	0.261 ± 0.046	0.318 ± 0.081	0.0030 ± 0.0007	0.0091 ± 0.0110	0.233 ± 0.052	0.300 ± 0.084
512	0.0039 ± 0.0012	0.0151 ± 0.0165	0.327 ± 0.051	0.400 ± 0.078	0.0074 ± 0.0024	0.0274 ± 0.0281	0.341 ± 0.049	0.413 ± 0.079

renormalize the batch, resulting in a new batch brightness distribution. If our new distribution is as desired, we stop. Otherwise, we iterate the process until convergence.

## G Additional Measurements of the Quality of Our Reconstructed Images

In Sec. 5 and App. C.2, we focussed on reporting the quality of our image reconstructions in terms of the popular PSNR image quality metric. In this section, we provide additional image quality measurements in terms of the mean square error of the individual pixels (*MSE*) and the learned perceptual image patch similarity (*LPIPS*) metrics. We present the additional measurements for all single-batch experiments from App. C.2 in Table 6 and Table 7 for CIFAR10 and CIFAR100, respectively. Further, in Table 8, we present the additional measurements for the multi-client experiments originally presented in Sec. 5. The additional measurements reinforce our observations from Sec. 5 that SEER consistently reconstructs client data well.

## H Comparison between Properties $\mathcal{P}$ based on Global and Local Distributions

In this section, we compare our two SEER variants based on local and global properties  $\mathcal{P}$ , respectively. We mount both variants of SEER on gradients coming from a single client with batch size  $B = 128$  on CIFAR10. We note that both methods are well-defined in this setting, and either one can successfully reconstruct data from the client batches, however, the global one is probabilistic in nature.

The results are depicted in Table 9. While both methods successfully reconstruct the majority of client batches, we clearly see the benefits of using the local property  $\mathcal{P}$ . In particular, the results in Table 9 suggest that the local distribution approach reconstructs up to 1.75 times more images, while also producing higher PSNR values not only on the full set of reconstructed batches but also on the top 37% of them. This motivates the need for our single-client attack, which demonstrates that secure aggregation provides additional protection to individual clients.

Table 8: Multi-client reconstruction on the bright and dark properties using different number of clients  $C$  on CIFAR10, for different total numbers of points. We report additional reconstruction quality measures—the average MSE (*MSE Top*) and LPIPS (*LPIPS Top*) and their respective standard deviations on the top 37% images.

#Pts	$C = 4$ , Dark		$C = 4$ , Bright		$C = 8$ , Dark		$C = 8$ , Bright	
	MSE Top $\downarrow$	LPIPS Top $\downarrow$						
64	0.0020 $\pm$ 0.0013	<b>0.110 <math>\pm</math> 0.052</b>	0.0027 $\pm$ 0.0022	<b>0.091 <math>\pm</math> 0.060</b>	0.0031 $\pm$ 0.0023	<b>0.111 <math>\pm</math> 0.059</b>	<b>0.0026 <math>\pm</math> 0.0021</b>	0.123 $\pm$ 0.073
128	0.0018 $\pm$ 0.0013	0.130 $\pm$ 0.050	0.0028 $\pm$ 0.0018	0.105 $\pm$ 0.064	0.0028 $\pm$ 0.0023	0.118 $\pm$ 0.070	0.0031 $\pm$ 0.0026	<b>0.111 <math>\pm</math> 0.075</b>
256	<b>0.0012 <math>\pm</math> 0.0008</b>	0.130 $\pm$ 0.045	<b>0.0022 <math>\pm</math> 0.0012</b>	0.113 $\pm$ 0.049	0.0023 $\pm$ 0.0014	0.130 $\pm$ 0.060	0.0035 $\pm$ 0.0022	0.164 $\pm$ 0.085
512	<b>0.0012 <math>\pm</math> 0.0008</b>	0.142 $\pm$ 0.054	0.0030 $\pm$ 0.0013	0.208 $\pm$ 0.064	<b>0.0015 <math>\pm</math> 0.0010</b>	0.159 $\pm$ 0.054	0.0029 $\pm$ 0.0017	0.170 $\pm$ 0.074

Table 9: Single-client reconstruction on bright and dark properties from batches of size  $B = 128$  on CIFAR10 using our Single-client method (*Local*) and our Secure Aggregation method with  $C = 1$  (*Global*). We report the percentage of well-reconstructed images (*Rec*), the average PSNR and its standard deviation across all reconstructions (*PSNR All*), and across the top 37% images (*PSNR Top*).

$\mathcal{P}$	CIFAR10, Bright			CIFAR10, Dark		
	Rec (%)	PSNR Top	PSNR All	Rec (%)	PSNR Top	PSNR All
Global	54.4	27.0 $\pm$ 1.8	20.6 $\pm$ 5.8	61.9	27.7 $\pm$ 2.2	21.1 $\pm$ 6.1
Local	<b>94.2</b>	<b>31.9 <math>\pm</math> 1.7</b>	<b>28.2 <math>\pm</math> 4.3</b>	<b>74.5</b>	<b>29.5 <math>\pm</math> 1.4</b>	<b>23.6 <math>\pm</math> 6.2</b>